

Strong-field induced XUV transmission and multiplet splitting in $4d^{-1}6p$ core-excited Xe studied by femtosecond XUV transient absorption spectroscopy

Ming-Fu Lin,^{1,2} Adrian N. Pfeiffer,^{1,2} Daniel M. Neumark,^{1,2} Stephen R. Leone,^{1,2,3} and Oliver Gessner¹

¹Ultrafast X-ray Science Laboratory, Chemical Sciences Division, Lawrence Berkeley National Laboratory, Berkeley, California 94720, USA

²Department of Chemistry, University of California at Berkeley, Berkeley, California 94720, USA

³Department of Physics, University of California at Berkeley, Berkeley, California 94720, USA

(Received 25 August 2012; accepted 30 November 2012; published online 28 December 2012)

Light-induced coupling of core-excited states of Xe atoms is investigated by femtosecond extreme ultraviolet (XUV) transient absorption spectroscopy with photon energies ranging from 50 eV to 72 eV. Coupling of the $4d^{-1}(^2D_{5/2})6p(^2P_{3/2})$ (65.1 eV) and $4d^{-1}(^2D_{3/2})6p(^2P_{1/2})$ (67.0 eV) core-excited states to nearby states by a strong infrared laser field leads to a threefold enhancement of XUV transmission. The transmission at 65.1 eV (67.0 eV) changes from $3.2 \pm 0.4\%$ ($5.9 \pm 0.5\%$) without the coupling laser to $9 \pm 2\%$ ($22 \pm 5\%$) at the maximum of the laser field. A strong-field induced broad XUV absorption feature between 60 eV and 65 eV is ascribed to splitting of the field-free absorption lines into multiple branches when the Rabi frequencies of the coupling transitions exceed the infrared laser frequency. This picture is supported by a comparison of the strong-field induced absorption spectrum with a numerical integration of the von Neumann equation for a few-level quantum system. The valence hole-alignment of strong-field ionized Xe is revisited, confirming the previously observed reduced alignment compared to theoretical predictions. © 2012 American Institute of Physics. [<http://dx.doi.org/10.1063/1.4772199>]

I. INTRODUCTION

Optical control of the properties of matter in the extreme ultraviolet (XUV) energy regime is an active field of research.^{1–8} In the infrared (IR), visible, and ultraviolet, light induced manipulation of the optical properties of matter has been demonstrated by a wide variety of effects, including coherent population trapping,⁹ Autler-Townes splitting,¹⁰ electromagnetically-induced transparency (EIT),^{11–13} lasing without inversion,¹⁴ and “stopping” of light.¹⁵ All of these phenomena can be described and understood in the picture of light-coupled few-level quantum systems.^{13,16} However, there are fundamental differences between strong-field control mechanisms in the optical and the XUV regimes that arise from different lifetimes of the relevant electronic states. The XUV probe field can induce transitions into core-hole states or doubly-excited states that have lifetimes of only a few femtoseconds. As a consequence, the NIR field must be extraordinarily strong to induce coherent coupling. Femtosecond laser pulses can achieve the necessary field strengths, but the laser field becomes so strong that it couples the excited states to the ionization continuum by multiphoton ionization,⁸ tunneling ionization,¹⁷ or Coulomb-barrier suppression.¹⁸ It is therefore important to gain a detailed understanding of strong-field induced coupling and ionization effects in highly excited states in order to be able to manipulate the optical properties of matter in the XUV in a controlled fashion.

Transient XUV absorption experiments, where the delay between the coupling pulse and the probe pulse is scanned

while the transmitted spectrum of the probe pulse is recorded, are particularly well suited to study the physics that governs strong-field induced ionization and the coupling of core-excited states.^{2,19,20} In this work, an ultrafast XUV transient absorption measurement on Xe atoms exposed to an intense NIR laser field is performed using broadband femtosecond XUV pulses with photon energies extending from 50 eV to 72 eV. The XUV pulses are generated by high harmonic generation (HHG). The inherent broadband nature of HHG light eliminates the need to scan the probe frequency, enabling laboratory-based XUV transient absorption experiments despite the relatively modest photon fluence of HHG based light sources. The impact of the NIR laser field on the electronic structure and the XUV optical properties of Xe is traced by changes in the XUV absorption spectrum as a function of the delay between the XUV probe pulse and the NIR coupling pulse. The measurements reveal a variety of effects such as strong-field induced XUV transmission and absorption, NIR coupling induced multiplet splitting, and core-hole alignment in strong-field ionized atoms.

Strong-field induced transmission and absorption are observed for photon energies in the vicinity of the transitions from the 1S_0 ground state to the $4d^{-1}(^2D_{5/2})6p(^2P_{3/2})$ and $4d^{-1}(^2D_{3/2})6p(^2P_{1/2})$ core-excited states of atomic Xe at 65.1 eV and 67.0 eV, respectively. The most prominent features can be described by the near-resonant coupling of the $4d^{-1}6p$ states to nearby $4d^{-1}6s$ and $4d^{-1}6d$ states (Autler-Townes doublet).^{1,21} Near the peak of the NIR field, additional absorption features are observed in the spectral region

between 60 eV and 65 eV. These features can principally be modeled by either near-resonant or off-resonant coupling to neighboring Rydberg states at sufficiently high coupling field intensities such that the Rabi frequencies of the coupling transitions exceed the NIR frequency.²² Under these conditions, the field-free absorption lines split into multiple branches, spanning a range between 62 eV and 65 eV at the low energy side of the field-free resonances. As a specific showcase example for this effect, theoretical evidence for multiple branches in near-resonant Autler-Townes splitting is presented by numerical integration of the von Neumann equation. The results indicate that the light-induced absorption between 60 eV and 62 eV may be due to a breakdown of the rotating wave approximation (RWA).²²

Furthermore, the alignment of the $5p^{-1}$ valence hole of Xe^+ ions created by strong-field ionization is revisited. Femtosecond transient XUV absorption spectroscopy has previously been used as a powerful tool to probe the electronic alignment of cationic states of atoms created by strong-field ionization.^{19,20,23} In this work, the measured degree of hole-alignment for the transitions at 55.4 eV and 57.3 eV is in reasonable agreement with previous experiments and, in particular, confirms a lower degree of alignment than predicted by theory.^{19,24}

II. EXPERIMENTAL METHODS

The XUV transient absorption spectroscopy setup is shown in Fig. 1. The laser is a commercial high power femtosecond laser system that provides pulses with a center wavelength of 775 nm. For the transient absorption experiments in this study, the grating compressor of the laser system is adjusted to chirp the laser pulse. This detuning leads to a broadening of discrete harmonics in order to generate a quasi-continuous HHG spectrum²⁵ with photon energies that span a wide range of the Xe $4d^{-1}$ inner shell absorption spectrum. It also results in a temporal broadening of the coupling pulse to 100 ± 10 fs (FWHM).

A 50/50 beam splitter is used to split the original NIR pulse into a “pump” pulse for strong-field coupling and ionization and the driver pulse for HHG, which produces the XUV “probe” pulse. HHG is performed in a 25 mm long gas cell filled with neon gas at a pressure of 3.33 kPa, tuned for

optimal phase matching.²⁶ The 1.3 mJ HHG driving pulses are focused to a $90 \mu\text{m}$ ($1/e^2$) spot size with an $f/30$ lens. A 300 nm thick aluminum foil is used to remove the residual NIR light from the XUV pulse. A toroidal mirror is used to focus the transmitted XUV light into the interaction region inside a 3 mm long target cell filled with xenon gas at a pressure of 2.53 kPa. The beam diameter ($1/e^2$) of the XUV light in the interaction region is $100 \pm 10 \mu\text{m}$. After passing through the absorption cell, the XUV light is dispersed by a constant line spacing spherical grating (1200 lines/mm) and detected by a chevron-mounted pair of microchannel plates (MCPs) coupled to a phosphor screen. The resulting two-dimensional image is read out by a CCD camera and then transferred to a computer for analysis. The XUV flux at the entrance of the absorption cell is $\sim 10^5$ photons per pulse in the spectral region between 50 eV and 72 eV.

The NIR pump pulse is focused into the target cell by an $f/40$ lens. The pump and probe pulses are combined by an annular mirror that is placed in front of the target cell. The XUV probe beam passes through the center hole of the mirror, while the NIR pump beam is reflected by the mirror to achieve pump-probe overlap in the interaction volume. The angle between the pump and probe beams is approximately 1.3° . The measured beam diameter ($1/e^2$) of the focused NIR beam at the target cell position is $150 \pm 10 \mu\text{m}$. This results in a peak intensity of the NIR pump beam on the order of 10^{14} W/cm². The estimated NIR peak intensities are 0.5×10^{14} W/cm² for the induced XUV transmission/absorption measurements and 1×10^{14} W/cm² for valence hole-alignment measurements.

The experimental energy resolution is derived by modeling the static field-free XUV absorption spectrum of xenon atoms through a convolution of the literature spectrum^{27–29} with Gaussian functions. The peaks in Fig. 2(a) correspond to inner-shell excitations from the $1S_0$ ground state to the $4d^{-1}(^2D_{5/2})6p(^2P_{3/2})$, $4d^{-1}(^2D_{5/2})7p(^2P_{3/2})$, and $4d^{-1}(^2D_{3/2})6p(^2P_{1/2})$ core-excited states at energies of 65.1 eV, 66.3 eV, and 67.0 eV, respectively.^{27,28,30,31} The experimental data are shown as vertical lines that represent the error bars. The solid line represents the model described above, corresponding to an instrumental energy resolution of 0.37 eV.

An upper bound of 70 fs for the duration of the chirped XUV pulse is derived from the rise time of the strong-field ionization signal. Fig. 2(b) shows the pump-probe time-delay dependent change in the XUV absorbance at 55.4 eV, corresponding to the emergence of the $(5p_{3/2}^{-1})^2P_{3/2} \rightarrow (4d_{5/2}^{-1})^2D_{5/2}$ transition in xenon ions that are created by strong-field ionization.³² Here, nl_j^{-1} represents a valence hole in the nl orbital with total angular momentum j . Fitting the absorption trace with an error function leads to a rise time of 70 ± 10 fs.

The transient spectra shown in Secs. III and IV are obtained by using spectra collected at -280 fs delay time as a reference delay.³³ Zero delay between pump and probe pulses is defined by the maximum induced transmission of the neutral xenon signal at 67.0 eV. A positive time delay corresponds to a pulse sequence where the NIR pump pulse arrives at the sample before the XUV probe beam. A half-wave plate is placed into the path of the pump beam to vary the relative polarization of pump and probe beams in the ion alignment

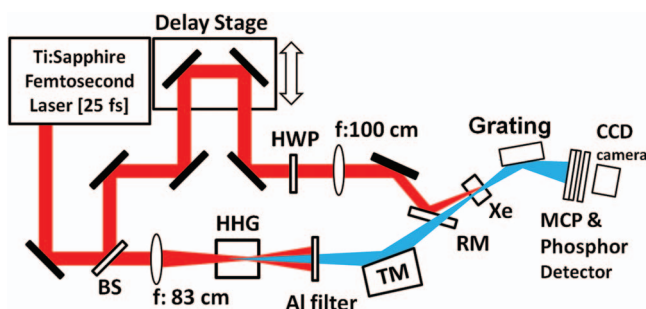


FIG. 1. Apparatus for transient XUV absorption experiments. Red and blue colors represent the NIR and XUV beams, respectively. BS: beam splitter, HHG: high harmonic generation cell, TM: toroidal mirror, HWP: half wave plate, RM: recombination mirror, and MCP: microchannel plates.

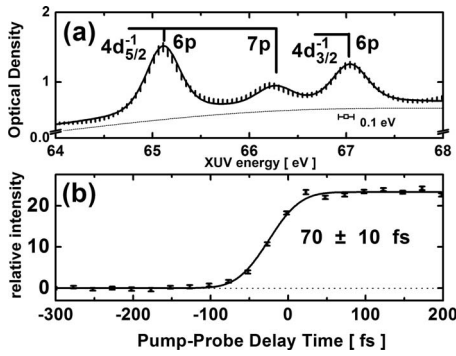


FIG. 2. (a) Absorption peaks due to transitions to different core-excited states of neutral xenon. The vertical bars correspond to the experimental data with error bars. The solid black line represents the simulated absorption profile using a natural linewidth of 0.11 eV (Refs. 27, 28, and 30) convoluted with the instrumental energy resolution of 0.37 eV. The broad thin line represents a non-resonant background due to ionization. Its contribution to the spectrum in (a) is estimated by a broad Gaussian peak that is centered at the maximum of the $\text{Xe}^+(4d^{-1})$ giant resonance and for which the ratio of OD's at 64.4 eV and 67.8 eV is the same as the ratio between the ionization cross sections at these energies.^{28,30} (b) Emergence of xenon ions monitored by the transient absorption signal at 55.4 eV corresponding to the $(5p_{3/2}^{-1})^2 P_{3/2} \rightarrow (4d_{5/2}^{-1})^2 D_{5/2}$ transition in Xe^+ . The solid line is the result of a fit to an error function, giving a rise time of 70 ± 10 fs (FWHM). See text for details.

experiments. The experimentally confirmed polarization purity of the NIR beam is $\geq 100:1$. The uncertainty of the relative angle between the pump and probe beam polarizations in the interaction volume is $\pm 2^\circ$. It is determined by using a combination of a polarizer and a half-wave plate independently for both the NIR pump beam and the NIR driver of the XUV probe beam at the location of the interaction volume. The NIR driver and XUV probe beam polarizations are parallel by virtue of the HHG process in an isotropic medium.³⁴ The error bars in all figures denote 95% confidence intervals unless otherwise noted.

III. RESULTS

A. Laser induced absorption, transmission, and ionization

Fig. 3(a) shows the static absorption spectrum of neutral xenon from a synchrotron based study.²⁹ The peaks at 65.1 eV and 67.0 eV (marked with asterisks) correspond to transitions from the 1S_0 ground state to the $4d^{-1}(^2D_{5/2})6p(^2P_{3/2})$ and $4d^{-1}(^2D_{3/2})6p(^2P_{1/2})$ core-excited states, respectively, that decay to form Xe^+ and Xe^{2+} ions.³⁰ Fig. 3(b) displays the NIR induced time- and energy-resolved change in the XUV optical density of the gas cell (ΔOD). The quantity ΔOD is defined in Eq. (1) as the difference in optical density with and without laser dressing. The latter condition is represented by data recorded at a large negative delay $t_{ref} = -280$ fs in order to account for a small constant background from scattered NIR light.³³ This background signal could not be completely eliminated in the experiment. It is taken into account in the analysis by using the spectrum that is recorded when the XUV pulse precedes the NIR pulse by 280 fs as a reference for the sum of the time-independent NIR background and the XUV spectrum without laser dressing. Modification

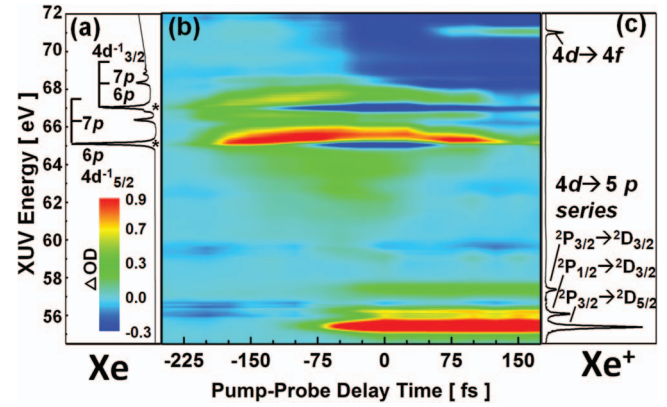


FIG. 3. (a) Static absorption spectrum of neutral Xe atoms from a previous study,²⁹ containing two different spin-orbit series of $4d^{-1} \rightarrow np$ inner shell excitations.^{27,28,30} (b) Transient XUV absorption spectra of neutral and ionized xenon atoms. The time- and energy-resolved change in the XUV optical density (ΔOD) reveals that the NIR pump pulse simultaneously induces both enhanced absorption ($\Delta\text{OD} > 0$) and enhanced transmission ($\Delta\text{OD} < 0$) in the vicinity of 65.1 eV and 67.0 eV. (c) Static photoionization yield spectrum of Xe^+ ions in the range of $4d^{-1} \rightarrow 5p, 4f$ inner-shell excitations.³²

of the NIR background by XUV absorption can be neglected since the number of core-excited Xe atoms ($< 10^5$) is ten orders of magnitude lower than the number of NIR photons ($\sim 10^{15}$ /pulse).

$$\begin{aligned} \Delta\text{OD}(t) &= \log \left[\frac{I(t_{ref})}{I(t)} \right] = \log \left[\frac{I_0}{I(t)} \right] - \log \left[\frac{I_0}{I(t_{ref})} \right] \\ &= \text{OD}(t) - \text{OD}(t_{ref}). \end{aligned} \quad (1)$$

Here, I_0 represents the transmitted XUV intensity without Xe gas and the dressing NIR field. $I(t)$ and $I(t_{ref})$ denote the transmitted XUV intensity with Xe gas in the target cell at pump-probe delays of t and $t_{ref} = -280$ fs, respectively. Note that at $t_{ref} = -280$ fs, the XUV and NIR pulses have no temporal overlap. For a thin target, ΔOD is linearly proportional to the product of the number density of transient species and their absorption cross section. Fig. 3(c) shows the photoionization yield spectrum of Xe^+ ions.³² The absorption peaks at 55.4 eV, 56.2 eV, and 57.3 eV correspond to the $4d$ inner-shell to $5p$ valence hole excitations $5p_{3/2}^{-1}(^2P_{3/2}) \rightarrow 4d_{5/2}^{-1}(^2D_{5/2})$, $5p_{1/2}^{-1}(^2P_{1/2}) \rightarrow 4d_{3/2}^{-1}(^2D_{3/2})$, and $5p_{3/2}^{-1}(^2P_{3/2}) \rightarrow 4d_{3/2}^{-1}(^2D_{3/2})$, respectively. The absorption peak at 71 eV has previously been assigned to a $4d \rightarrow 4f$ transition in Xe^+ .^{32,35}

The transient absorption data in Fig. 3(b) reveal that the NIR pump pulse simultaneously induces both enhanced absorption ($\Delta\text{OD} > 0$) and enhanced transmission ($\Delta\text{OD} < 0$) in the vicinity of the neutral xenon XUV absorption resonances. The split features at 65.1 eV to 67.0 eV extend significantly toward negative (XUV first) pump-probe time delays. The strong-field induced absorption features associated with transitions involving $6p$ excitations obscure minor features from absorption to the $7p$ state at 66.3 eV. The extended absorption feature between 60 eV and 65 eV does not have a direct correspondence to features in the static absorption spectra. Their origin will be discussed in Sec. IV A. The narrow enhanced transmission features at 56.4 eV, 59.6 eV,

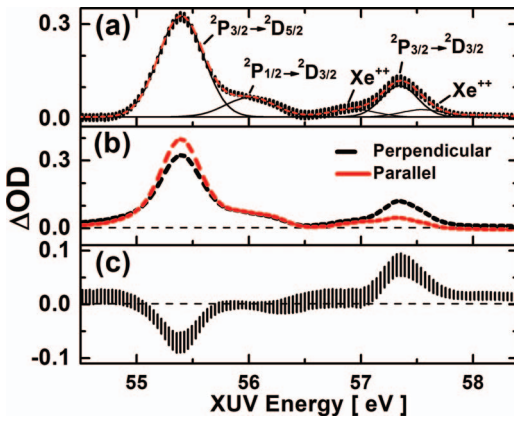


FIG. 4. Xe^+ ion absorption spectra for different relative polarizations of the NIR and XUV pulses. The spectra are averaged over pump-probe delays between 25 fs and 250 fs. (The ion signals in this energy range are constant for delays beyond 25 fs.) (a) Perpendicular polarization of XUV and NIR laser field. The underlying spectra contain contributions from singly and doubly charged xenon ions. Black vertical bars represent the experimental data with error bars. The dashed red line is the sum of all individually fitted ionic species shown as black solid lines. (b) Polarization dependence of xenon ion absorption spectra. Red dashed and black dashed lines are measured with parallel and perpendicular polarizations of the XUV and NIR fields, respectively. (c) Difference of spectra in (b). Note the opposite signs at 55.4 eV and 57.3 eV.

62.8 eV, 69 eV, and 72 eV are artifacts due to small denominator values in Eq. (1). These are caused by small high harmonic intensities in the minima of the HH spectrum, which exhibit the same energy spacing as the HH maxima (3.2 eV).

Fig. 3(b) also shows the emergence of xenon ions for positive pump-probe delays as a consequence of strong-field ionization by the NIR pump pulse. Note that strong-field ionization is a nonlinear process, which leads to a delayed onset of the ion signals below 58 eV compared to the signals from the neutral excited states above 60 eV. The deep blue area spanning 67 eV to 72 eV for positive delays is due to depletion ($\Delta OD < 0$) of neutral xenon atoms by strong-field ionization. The emergence of the Xe^+ ion signal at 71 eV exhibits a 70 fs delay relative to the ion signals at other energies. The generated ions include singly and doubly charged states as can be seen in Fig. 4(a). All spectra in Fig. 4 are generated by averaging the transient absorption data over a delay range of 25 fs to 250 fs. The ion signals between 55 eV and 58 eV reach their asymptotic values at a delay of 25 fs. Three spin-orbit transitions involving the promotion of an electron from a $4d$ orbital to a $5p$ hole of Xe^+ can be seen at 55.4 eV, 56.2 eV, and 57.3 eV. Minor contributions from transitions in Xe^{2+} ions are also shown. Fig. 4(b) shows the same spectral features as Fig. 4(a) recorded for parallel (red) and perpendicular (black) alignment of the NIR and XUV polarizations at a nominal NIR power density of 10^{14} W/cm². The transition intensities at 55.4 eV and 57.3 eV exhibit a strong polarization dependence with opposite signs as illustrated by the difference plot in Fig. 4(c). No polarization dependence is observed for the transition at 56.2 eV, as expected for a $J = 1/2$ state.¹⁹

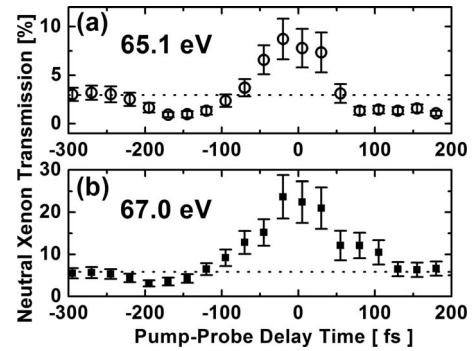


FIG. 5. Laser-induced transmission of neutral xenon at 65.1 eV and 67.0 eV after correcting for the depletion in the pump-probe interaction volume due to strong-field ionization. (a) $4d^{-1}(^2D_{5/2})6p(^2P_{3/2})$ core-excited state at 65.1 eV. (b) $4d^{-1}(^2D_{3/2})6p(^2P_{1/2})$ core-excited state at 67.0 eV. The transmission far from time zero is described by the optical density of xenon atoms in a field-free environment. While approaching the maximum of the NIR envelope, the transmission increases gradually by a factor of three.

B. NIR-induced transmission in the XUV regime

The strong NIR field manipulates the electronic properties of the Xe atoms, which results in a change of XUV transmission at 65.1 eV ($4d^{-1}(^2D_{5/2})6p(^2P_{3/2})$) and 67.0 eV ($4d^{-1}(^2D_{3/2})6p(^2P_{1/2})$) through field-induced coupling among core-excited states. The field-strength dependent effect of the NIR pump pulse on the core-excited states is obtained by monitoring the change of transmission at the field-free resonance energies. The time-dependent transmission curves, after correcting for neutral xenon depletion by strong-field ionization,³⁶ are shown in Fig. 5. Long before time zero, the constant transmission is determined by the field-free neutral xenon absorbance as shown in Fig. 2(a). The transmittance at 67.0 eV returns to its field-free value at long time delays, while at 65.1 eV it is slightly lower due to a residual effect of the NIR at the longest time delays as can be seen in Fig. 3(b). The NIR laser field changes the transmission at 65.1 eV and 67.0 eV from $3.2 \pm 0.4\%$ and $5.9 \pm 0.5\%$ (field-free) to $9 \pm 2\%$ and $22 \pm 5\%$, respectively, i.e., by approximately a factor of 3–4. The induced transmission curve in Fig. 5 approximately follows the NIR envelope. The width of the transmission curve in Fig. 5(b) is 100 ± 10 fs, which is longer than the xenon ion rise time of 70 ± 10 fs derived from the traces in Fig. 2. This effect is probably due to the nonlinear character of strong-field ionization and ionization saturation in the leading edge of the NIR pulse.

IV. ANALYSIS AND DISCUSSION

A. Simulation of light-induced line splitting

The induced transmission and absorption in the vicinity of the neutral xenon XUV absorption resonances are modeled in the framework of a few-level quantum system. The basis for the simulations is described in Refs. 22 and 37. In principle, both near-resonant coupling as well as off-resonant coupling to nearby core-excited states may contribute to the observed effects. Here, we discuss the specific example of near-resonant (Autler-Townes) coupling of the $4d^{-1}(^2D_{5/2})6p(^2P_{3/2})$ and $4d^{-1}(^2D_{3/2})6p(^2P_{1/2})$

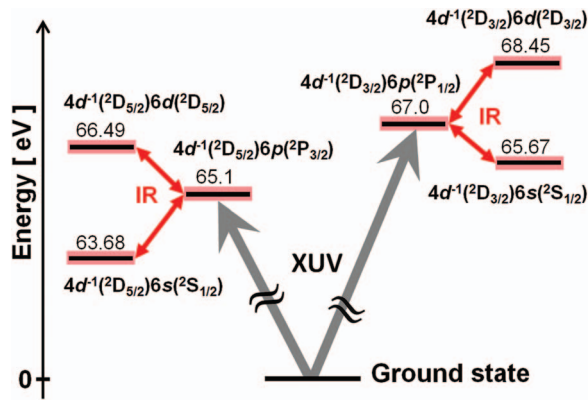


FIG. 6. Reduced level scheme for strong-field coupling. The left side of the figure shows the levels that are most important for the coupling of the $4d^{-1}(^2D_{5/2})6p(^2P_{3/2})$ core-excited states. On the right, the coupling levels for the $4d^{-1}(^2D_{3/2})6p(^2P_{1/2})$ core-hole state are shown. The vertical widths of the horizontal black and red bars represent the natural and effective linewidths, respectively. The numbers on the levels represent excitation energies in eV.

states to the $4d^{-1}(^2D_{5/2})6s(^2S_{1/2})$, $4d^{-1}(^2D_{3/2})6s(^2S_{1/2})$, $4d^{-1}(^2D_{5/2})6d(^2D_{5/2})$, and $4d^{-1}(^2D_{3/2})6d(^2D_{3/2})$ states by the intense NIR field (Fig. 6). This coupling scheme is expected to contribute significantly to the light-induced effects described above due to relatively large oscillator strengths and the near-resonant character of the NIR transitions. However, contributions from other transitions involving, for example, $7s$ states cannot be excluded. In Ref. 22, a Hamiltonian is introduced in the dipole approximation as shown in Eq. (2),

$$\mathbf{H} = \mathbf{H}_0 + \mathbf{D}F, \quad (2)$$

where \mathbf{H}_0 is the Hamiltonian of the unperturbed system, \mathbf{D} is the dipole transition matrix, and F is the electric field of the laser pulse. The parameters of the electric field are matched to the experimental conditions: the infrared pulse has a center wavelength of 775 nm and a transform limited pulse duration of 25 fs. A linear chirp is added such that the effective temporal duration is 100 fs. The peak intensity is 0.5×10^{14} W/cm². The XUV field is a pulse train consisting of 15 pulses, each with a duration of 0.1 fs and a center energy of 61 eV. The spatial intensity profile of the coupling laser is not included in the calculation.

Two cases are considered in the simulations in order to address the broad induced absorption feature in Fig. 3(b) that extends from 60 eV to 65 eV. First, as previously shown, the RWA is applied, such that F is replaced by the complex field values for the off-diagonal entries of \mathbf{H} and the rapidly oscillating terms are neglected.²² Second, no approximation is made with respect to the electric field. The absorbance is calculated from the density matrix assuming a thin gas target. The absorbance is predicted to show multiple lines for high field strengths,²² a phenomenon that can only be described without the RWA.

The simulation from Ref. 22 is generalized to include lifetime effects. The time evolution of the density matrix of the states is calculated by the numerical integration of the von-Neumann equation with the inclusion of phenomenological

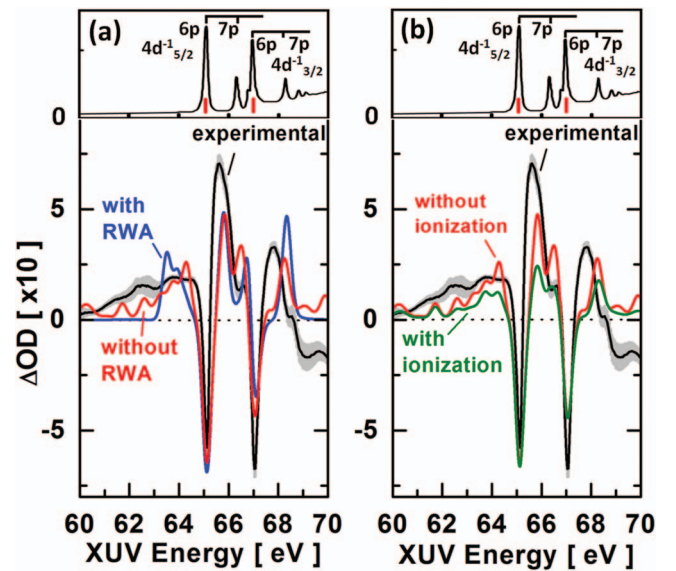


FIG. 7. Comparison of the experimental change in optical density ΔOD with simulations at a pump-probe delay of 0 fs. In (a) and (b), the top figures represent the field-free neutral xenon absorption spectrum from Ref. 29. In the bottom of (a) and (b), the black solid curve shows the experimental result where the statistical error is indicated by the grey area (2σ). (a) The simulations with and without the RWA are shown as blue and red curves, respectively, without the inclusion of ionization broadening. (b) The green and red curves show the simulation with and without ionization broadening, both without the assumption of the RWA. The simulated curves are convoluted with the experimental energy resolution of 0.37 eV.

decay rates as shown in Eq. (3).

$$i\dot{\rho} = [\mathbf{H}, \rho] + i\mathbf{\Gamma}, \quad (3)$$

where ρ is the density matrix and $\mathbf{\Gamma}$ is a matrix that contains the decay rates of the states. The decay matrix $\mathbf{\Gamma}$ accounts for the natural lifetime of the core-hole states and for strong-field ionization of the ground state. The inclusion of ionization broadening in the decay matrix of the core-excited states is discussed in the next section.

Fig. 7 shows a comparison of the experimental ΔOD (black curve) with the simulations, convoluted with the experimental energy resolution of 0.37 eV, at a pump-probe delay of 0 fs. In Fig. 7(a), the blue and red curves correspond to the simulations with and without the RWA, respectively. In both simulations, the $4d \rightarrow 6p$ transitions at 65.1 eV and 67.0 eV are split due to coupling to nearby $4d^{-1}6s$ and $4d^{-1}6d$ states. A significant difference between the simulations with (blue) and without (red) applications of the RWA in Fig. 7(a) is found in the spectral region between 60 eV and 65 eV. The simulation that makes use of the RWA exhibits a sharp cut-off at 63 eV, whereas the absorption features in the simulation without RWA extend down to 60 eV. A qualitative interpretation for this observation can be given if the level system is restricted even more to a three-level system. If only one XUV transition and one NIR coupling transition are considered, such as in Ref. 22, the field-free XUV absorption line is split into a doublet for moderate intensities, which is characteristic for Autler-Townes splitting in the visible regime. At higher intensities, for which the Rabi frequency exceeds the frequency of the coupling laser field, the NIR coupling

induces a multiplet splitting that is not captured within the RWA.²² For the core-excited states with the strongest coupling, $(4d^{-1}(^2D_{5/2})6p(^2P_{3/2}))$ and $(4d^{-1}(^2D_{5/2})6s(^2S_{1/2}))$, this condition is fulfilled for NIR intensities beyond 0.16×10^{14} W/cm².

In Fig. 7, the splitting due to coupling to the $4d^{-1}6s$ and $4d^{-1}6d$ states is so large that it exceeds the energy gap between the two $4d^{-1}6p$ states. Hence, the split peaks overlap and cannot be assigned to a specific XUV transition. The exact shape of the experimental ΔOD curve is not reproduced by the simulation. This finding is not surprising, because the simulation is based on a highly simplified level scheme where many electronic states are neglected. Additionally, the NIR intensity distribution across the interaction volume is neglected.

Due to the several contributing levels, the ΔOD curve does not exhibit clear side branches, but rather a variety of absorption features appear in the spectral region from 60 to 65 eV. This structure is qualitatively reproduced in the simulation without the RWA, whereas it is missed entirely if the RWA is made. The observation of side branches in the three-level system is not restricted to the lower energy side of the XUV absorption energy, but can also occur to the higher photon energy side.²² However, experimental observation in the higher photon energy regime is hindered by the contribution of higher lying Rydberg levels and the continuum (see Fig. 3(a)).

We also performed calculations based on coupling of the field-free core-excited states to other nearby states with, for example, $4d^{-1}7s$ electronic configurations. Discrete structures from off-resonant coupling have recently been observed in a combined experimental and theoretical study of atomic helium.³⁷ Qualitatively, the spectral features in all simulations are similar but differ in the magnitude of the energy splitting and the intensities of the light-induced structures. A common phenomenon, however, is that absorption features below 62 eV only emerge from calculations that go beyond the RWA, indicating that the observed absorption features in this energy range may indicate a breakdown of this frequently applied approximation.

B. The influence of ionization broadening

Under the influence of the strong NIR field, the dressed core-excited states are expected to have a shorter lifetime and thus a broader resonant linewidth.³⁸ In the absence of theoretical values, this broadening is estimated by the contribution of strong-field ionization of the core-excited states.

The estimate of the effective linewidth is based on a study of neon atoms,^{1,21} where the effective lifetime of the core-excited states $1s^{-1}3s$ ($1s^{-1}3p$) at a field intensity of 10^{13} W/cm² is 0.54 eV (0.68 eV), and the field-free core-hole linewidths are 0.27 eV (2.4 fs). The contribution of the laser ionization process in neon is estimated to be 0.54 (0.68) eV – 0.27 eV = 0.27 eV (0.41 eV) for the $1s^{-1}3s$ ($1s^{-1}3p$) core-excited states, respectively. The ionization potential (IP) of the $1s^{-1}3s$ ($1s^{-1}3p$) core-hole state is 4.54 eV (2.85 eV). These IP's are similar to the IP's of the core-excited states of xenon.²⁷ Therefore, we adapt the values from neon to ad-

dress the ionization broadening of the core-excited states in xenon. For lower field strengths, the contribution of the laser ionization process is calculated from ADK tunneling ionization rates.¹⁷ For higher field strengths, where the ADK rates exceed the ionization broadening that was calculated from the neon study, the values from the neon study are set as high field limits for the ionization broadening of xenon atoms. This approach is similar to the one applied in the work by Loh *et al.*²

In Fig. 7(b), the results of the non-RWA simulations with (green) and without (red) additional broadening due to the laser ionization of the core-hole states are shown. It can be seen that the impact of the additional broadening mechanism on the extended absorption features in the energy region from 60 to 65 eV is relatively small. Studies including more levels will be valuable to determine if better agreement could be achieved.

C. Hole alignment of xenon ions generated by strong-field ionization

We briefly revisit the hole-alignment in xenon ions generated by strong-field ionization.¹⁹ Note that only ionization from the electronic ground state has to be taken into account because the number of XUV photons is very small and therefore very few ions are produced by the XUV excitation of $6p$ states and subsequent ionization by the NIR light. Mechanisms leading to multiply charged ions are also neglected because their yield is very low in this experiment.

By definition, the $5p^{-1}_{1/2}$ ($^2P_{1/2}$) ionic state cannot exhibit any orbital alignment since it has only two magnetic sublevels $m_J = \pm 1/2$.³⁹ However, for the case of $J = 3/2$, theory predicts a greater population in the $m_J = \pm 1/2$ sublevels than in the $m_J = \pm 3/2$ sublevels of the $5p^{-1}_{3/2}$ ($^2P_{3/2}$) hole state.^{19,20,23,24} In order to compare the theoretical predictions with the experiment, the parameters shown in Eqs. (4a) through (4e) are derived from standard angular momentum algebra.

$$R = \frac{I_{\parallel} - I_{\perp}}{I_{\parallel} + 2I_{\perp}}, \quad (4a)$$

$$R_1 = \frac{1}{10} \frac{\rho_{3/2,|\pm 1/2|} - \rho_{3/2,|\pm 3/2|}}{\rho_{3/2,|\pm 1/2|} + \rho_{3/2,|\pm 3/2|}}, \quad (4b)$$

$$R_2 = 0, \quad (4c)$$

$$R_3 = \frac{2}{5} \frac{\rho_{3/2,|\pm 3/2|} - \rho_{3/2,|\pm 1/2|}}{\rho_{3/2,|\pm 3/2|} + \rho_{3/2,|\pm 1/2|}}, \quad (4d)$$

$$r = \frac{I_{3/2 \rightarrow 5/2}}{I_{1/2 \rightarrow 3/2}} = 1.6 \frac{3\rho_{3/2,|\pm 1/2|} + 2\rho_{3/2,|\pm 3/2|}}{5\rho_{1/2,|\pm 1/2|}}. \quad (4e)$$

Equation (4a) denotes the absorption anisotropy for the two different polarization schemes obtained from the experimental results. In Eqs. (4b) to (4d), R_1 , R_2 , and R_3 represent the polarization anisotropies for transitions at 55.4 eV, 56.2 eV, and 57.3 eV, respectively. The r value in Eq. (4e) denotes the ratio of the transition strengths at 55.4 eV and 56.2 eV.¹⁹

TABLE I. Hole-alignment in xenon ions. Comparison of quantum state distributions retrieved from the measured polarization anisotropies at 55.4 eV and 57.3 eV, results from Loh. *et al.* at 55.4 eV and the theoretical calculation in Ref. 19. The error bars in this work are the statistical errors of 95% confidence intervals after propagating through Eq. (4).

Quantum states	This work (55.4 eV/57.3 eV)	Loh <i>et al.</i> (55.4 eV)	Theoretical calculation
$\rho_{3/2, \pm 3/2\rangle}$	$26/17 \pm 9$	13 ± 6	3
$\rho_{3/2, \pm 1/2\rangle}$	$60/69 \pm 9$	75 ± 6	83
$\rho_{1/2, \pm 1/2\rangle}$	$14/14 \pm 2$	12 ± 3	14

$\rho_{J,|\pm m\rangle}$ is the probability of finding the xenon ion in a $5p_{J,mJ}$ or $5p_{J,-mJ}$ hole state.¹⁹ Note that according to the theory of tunneling ionization with the inclusion of spin-orbit coupling, $\rho_{3/2,|\pm 1/2\rangle}$ is larger than $\rho_{3/2,|\pm 3/2\rangle}$.^{19,20,23,24} The values for R_1 , R_3 , and r obtained from the data shown in Fig. 4 are 0.04 ± 0.02 , -0.24 ± 0.08 , and 5.5 ± 0.6 , respectively. The quantum state distributions for the resonances at 55.4 eV and 57.3 eV are shown in Table I along with the experimental results of Loh *et al.* at 55.4 eV and a theoretical calculation.¹⁹

The quantum state distribution derived from R_1 and R_3 in this work is similar to the one measured by Loh *et al.* with $R_1 = 0.07 \pm 0.01$. Both experiments yield a lower degree of alignment than predicted by theory with the inclusion of spin-orbit interaction.^{19,20} The discrepancy between theory and experimental results cannot be explained by the finite degree of linear polarization in the experiment ($\geq 100:1$) or the small uncertainty ($\pm 2^\circ$) in the relative angle between the pump and probe beam polarizations. A 2° mismatch between the polarization axes would lead to a lowering of the intensity ratio R_1 from the predicted value $R_1 = 0.0930$ to a measured value $R_1 = 0.0928$. The relative angle between the polarization axes would have to be off by 32° , i.e., more than an order of magnitude beyond the experimental uncertainty, to explain the difference between the predicted value of R_1 and the measured value $R_1 = 0.04$.

Loss of alignment through electron-ion collisions seems unlikely. Taking the value of electron-ion collision induced spin-orbit state transitions for similar quantum states in krypton ions,⁴⁰ the estimated dealignment time constant for Xe ions would be on the order of 15 ps at 2.53 kPa of xenon in the gas cell. Therefore, dealignment from electron-ion collisions within 300 fs is negligible. Other possible mechanisms for the loss of electronic alignment include a breakdown of the adiabatic approximation,^{19,23} multielectron effects,^{41,42} and re-collision of tunnel-ionized electrons with the parent ion core.^{43,44} Theoretical studies that go beyond the adiabatic approximation do not explain the lower degree of alignment.^{41,45} Thus, multielectron effects during the ionization and/or strong-field induced electron-ion recollision may be responsible for the lowering of the hole alignment of atomic xenon under strong-field ionization as observed in the experiments.

V. CONCLUSION

Femtosecond XUV transient absorption spectroscopy is employed to monitor the impact of an intense NIR pulse

on core-level transitions in xenon. Coupling of core-excited states by a strong NIR field induces both enhanced absorption and enhanced transmission around photon energies of 65.1 eV and 67.0 eV, corresponding to transitions from the ground state to $4d^{-1}(^2D_{5/2})6p(^2P_{3/2})$ and $4d^{-1}(^2D_{3/2})6p(^2P_{1/2})$ core-hole states, respectively. The threefold enhancement of XUV transmission by the NIR field leads to an ultrashort enhancement of the transmitted XUV light, effectively creating a “femtosecond XUV light switch.” This ability to control XUV pulses in the time domain may enable new possibilities for ultrafast pump-probe experiments at synchrotrons.^{1,3,4,21}

The observations are described in the picture of NIR-induced coupling between core-excited states within few-level quantum systems. Extended transient absorption features between 60 eV and 65 eV are interpreted as multiple absorption branches that emerge when the Rabi frequencies of the NIR coupling transitions exceed the NIR laser frequency. In particular, the example of Autler-Townes multiplet splitting due to near-resonant coupling of the $4d^{-1}6p$ core-excited states to $4d^{-1}6s$ and $4d^{-1}6d$ states is discussed in detail based on a numerical solution of the von Neumann equation. The results indicate that the rotating wave approximation for the description of the light-induced coupling breaks down for NIR peak intensities of $\sim 5 \cdot 10^{13}$ W/cm².

The strong NIR field also generates Xe⁺ ions in different fine-structure states, and the polarization anisotropy of the corresponding core level transitions is determined. The transition at 57.3 eV reveals an opposite polarization anisotropy, as expected, compared to the transition at 55.4 eV. The extracted quantum state distributions from the transitions at 55.4 eV and 57.3 eV both reveal a similar core-hole alignment as determined in previous measurements and a lower degree of alignment than predicted by theory.^{41,45}

ACKNOWLEDGMENTS

We thank Professor Zhi-Heng Loh, Dr. Scott Sayres, and Erik Hosler for discussions of alignment effects in strong-field ionized xenon. We appreciate Dr. Daniel Haxton’s help with respect to selection rules of atomic transitions. This work was supported by the Director, Office of Science, Office of Basic Energy Sciences, Chemical Sciences Division of the U.S. Department of Energy (Contract No. DE-AC02-05CH11231). A.N.P. is supported by the Laboratory Directed Research and Development Program at Lawrence Berkeley National Laboratory. S.R.L. acknowledges the support of a National Security Science and Engineering Faculty Fellowship. M.-F. Lin

expresses gratitude for the support of a fellowship from the Ministry of Education, Taiwan, Republic of China.

- ¹C. Buth, R. Santra, and L. Young, *Phys. Rev. Lett.* **98**, 253001 (2007).
- ²Z. H. Loh, C. H. Greene, and S. R. Leone, *Chem. Phys.* **350**, 7 (2008).
- ³T. E. Glover, M. P. Hertlein, S. H. Southworth, T. K. Allison, J. van Tilborg, E. P. Kanter, B. Krässig, H. R. Varma, B. Rude, R. Santra, A. Belkacem, and L. Young, *Nat. Phys.* **6**, 69 (2010).
- ⁴M. B. Gaarde, C. Buth, J. L. Tate, and K. J. Schafer, *Phys. Rev. A* **83**, 013419 (2011).
- ⁵M. Tarana and C. H. Greene, *Phys. Rev. A* **85**, 013411 (2012).
- ⁶W.-C. Chu and C. D. Lin, *Phys. Rev. A* **85**, 013409 (2012).
- ⁷W.-C. Chu, S.-F. Zhao, and C. D. Lin, *Phys. Rev. A* **84**, 033426 (2011).
- ⁸T. Mazza, K. G. Papamihail, P. Radcliffe, W. B. Li, T. J. Kelly, J. T. Costello, S. D. Diusterer, P. Lambropoulos, and M. Meyer, *J. Phys. B* **45**, 141001 (2012).
- ⁹E. Arimondo, *Prog. Opt.* **35**, 257 (1996).
- ¹⁰S. H. Autler and C. H. Townes, *Phys. Rev.* **100**, 703 (1955).
- ¹¹S. E. Harris, J. E. Field, and A. Imamoglu, *Phys. Rev. Lett.* **64**, 1107 (1990).
- ¹²K. J. Boller, A. Imamolu, and S. E. Harris, *Phys. Rev. Lett.* **66**, 2593 (1991).
- ¹³J. P. Marangos, *J. Mod. Opt.* **45**, 471 (1998).
- ¹⁴S. E. Harris, *Phys. Rev. Lett.* **62**, 1033 (1989).
- ¹⁵C. Liu, Z. Dutton, C. H. Behroozi, and L. V. Hau, *Nature (London)* **409**, 490 (2001).
- ¹⁶M. Fleischhauer, A. Imamoglu, and J. P. Marangos, *Rev. Mod. Phys.* **77**, 633 (2005).
- ¹⁷M. V. Ammosov, N. B. Delone, and V. P. Krainov, *Sov. Phys. JETP* **64**, 1191 (1986).
- ¹⁸S. Augst, D. D. Meyerhofer, D. Strickland, and S. L. Chint, *J. Opt. Soc. Am. B* **8**, 858 (1991).
- ¹⁹Z.-H. Loh, M. Khalil, R. E. Correa, R. Santra, C. Buth, and S. R. Leone, *Phys. Rev. Lett.* **98**, 143601 (2007).
- ²⁰E. Goulielmakis, Z. H. Loh, A. Wirth, R. Santra, N. Rohringer, V. S. Yakovlev, S. Zherebtsov, T. Pfeifer, A. M. Azzéer, M. F. Kling, S. R. Leone, and F. Krausz, *Nature (London)* **466**, 739 (2010).
- ²¹C. Buth and R. Santra, *Phys. Rev. A* **78**, 043409 (2008).
- ²²A. N. Pfeiffer and S. R. Leone, *Phys. Rev. A* **85**, 053422 (2012).
- ²³L. Young, D. A. Arms, E. M. Dufresne, R. W. Dunford, D. L. Ederer, C. Höhr, E. P. Kanter, B. Krässig, E. C. Landahl, E. R. Peterson, J. Rudati, R. Santra, and S. H. Southworth, *Phys. Rev. Lett.* **97**, 083601 (2006).
- ²⁴R. Santra, R. W. Dunford, and L. Young, *Phys. Rev. A* **74**, 043403 (2006).
- ²⁵X. Lavocat-Dubuis, F. Vidal, J. P. Matte, C. Popovici, T. Ozaki, and J. C. Kieffer, *Laser Part. Beams* **29**, 95 (2011).
- ²⁶E. J. Takahashi, Y. Nabekawa, H. Mashiko, H. Hasegawa, A. Suda, and K. Midorikawa, *IEEE J. Sel. Top. Quantum Electron.* **10**, 1315 (2004).
- ²⁷G. C. King, M. Tronc, F. H. Read, and R. C. Bradford, *J. Phys. B* **10**, 2479 (1977).
- ²⁸O. P. Sairanen, A. Kivimäki, E. Nömmiste, H. Aksela, and S. Aksela, *Phys. Rev. A* **54**, 2834 (1996).
- ²⁹R. Haensel, G. Keitel, P. Schreiber, and C. Kunz, *Phys. Rev.* **188**, 1375 (1969).
- ³⁰S. Osmekhin, M. Määttä, R. Sankari, J. Nikkinen, E. Kukkk, S. M. Huttala, S. Heinämäki, H. Aksela, and S. Aksela, *J. Phys. B* **38**, 3559 (2005).
- ³¹K. Codling and R. P. Madden, *Phys. Rev. Lett.* **12**, 106 (1964).
- ³²P. Andersen, T. Andersen, F. Folkmann, V. K. Ivanov, H. Kjeldsen, and J. B. West, *J. Phys. B* **34**, 2009 (2001).
- ³³Z.-H. Loh, M. Khalil, R. E. Correa, and S. R. Leone, *Rev. Sci. Instrum.* **79**, 073101 (2008).
- ³⁴P. Antoine, B. Carré, A. L'Huillier, and M. Lewenstein, *Phys. Rev. A* **55**, 1314 (1997).
- ³⁵M. Sano, Y. Itoh, T. Koizumi, T. M. Kojima, S. D. Kravis, M. Oura, T. Sekioka, N. Watanabe, Y. Awaya, and F. Koike, *J. Phys. B* **29**, 5305 (1996).
- ³⁶The asymptotic fraction of ionization is estimated by using absolute absorption cross-sections from the literature (Refs. 29 and 32) and absolute absorbance values (OD) for Xe and Xe⁺ measured in this work. Employing Beer's law, the asymptotic ionization fraction is determined to be ~14%. The time-dependent ionization fraction is modeled by scaling the pump-probe trace of Xe⁺ ions at 55.4 eV such that its intensity at the maximum delay matches the asymptotic ionization fraction.
- ³⁷S. Chen, M. J. Bell, A. R. Beck, H. Mashiko, M. Wu, A. N. Pfeiffer, M. B. Gaarde, D. M. Neumark, S. R. Leone, and K. J. Schafer, *Phys. Rev. A* **86**, 063408 (2012).
- ³⁸H. R. Varma, L. Pan, D. R. Beck, and R. Santra, *Phys. Rev. A* **78**, 065401 (2008).
- ³⁹R. N. Zare, *Angular Momentum: Understanding Spatial Aspects in Chemistry and Physics*, 1st ed. (Wiley-Interscience, 1988), p. 226.
- ⁴⁰C. Höhr, E. R. Peterson, N. Rohringer, J. Rudati, D. A. Arms, E. M. Dufresne, R. W. Dunford, D. L. Ederer, E. P. Kanter, B. Krässig, E. C. Landahl, R. Santra, S. H. Southworth, and L. Young, *Phys. Rev. A* **75**, 011403 (2007).
- ⁴¹N. Rohringer and R. Santra, *Phys. Rev. A* **79**, 053402 (2009).
- ⁴²A. E. Boguslavskiy, J. Mikosch, A. Gijsbertsen, M. Spanner, S. Patchkovskii, N. Gador, M. J. J. Vrakking, and A. Stolow, *Science* **335**, 1336 (2012).
- ⁴³H. Niikura, F. Legare, R. Hasbani, A. D. Bandrauk, M. Y. Ivanov, D. M. Villeneuve, and P. B. Corkum, *Nature (London)* **417**, 917 (2002).
- ⁴⁴P. B. Corkum, *Phys. Rev. Lett.* **71**, 1994 (1993).
- ⁴⁵R. Santra, V. S. Yakovlev, T. Pfeifer, and Z.-H. Loh, *Phys. Rev. A* **83**, 033405 (2011).